

Article

# Library of UV-Visible Absorption Spectra of Rare Earth Orthophosphates, $LnPO_4$ ( $Ln = La-Lu$ , except Pm)

Suchinder K. Sharma <sup>1,\*</sup> , Thomas Behm <sup>1</sup>, Thomas Köhler <sup>2</sup>, Jan Beyer <sup>1</sup> ,  
Richard Gloaguen <sup>3</sup>  and Johannes Heitmann <sup>1</sup>

<sup>1</sup> Institute of Applied Physics, TU Bergakademie Freiberg, Leipziger Str. 23, 09599 Freiberg, Germany; thomas.behm@physik.tu-freiberg.de (T.B.); jan.beyer@physik.tu-freiberg.de (J.B.); johannes.heitmann@physik.tu-freiberg.de (J.H.)

<sup>2</sup> Institute of Experimental Physics, TU Bergakademie Freiberg, Leipziger Str. 23, 09599 Freiberg, Germany; thomas.koehler@physik.tu-freiberg.de

<sup>3</sup> Helmholtz—Zentrum Dresden—Rossendorf, Helmholtz Institute Freiberg for Resource Technology, Chemnitz Str. 40, 09599 Freiberg, Germany; r.gloaguen@hzdr.de

\* Correspondence: suchindersharma@gmail.com; Tel.: +49-3731-39-2595

Received: 10 June 2020; Accepted: 7 July 2020; Published: 9 July 2020



**Abstract:** In recent times, rare earth orthophosphates ( $LnPO_4$ ) have shown great potential as efficient optical materials. They possess either *monazite* or *xenotime*-type structures. These light or heavy rare earth bearing orthophosphates also exhibit an extraordinary stability over geological time scale in nature,  $\sim 10^9$  years. In the present contribution, we measure, collect, and present a library of absorption spectra of all the  $LnPO_4$  hosts ( $Ln = La-Lu$ , except Pm) using their single crystal samples, to conclude that the observed spectral features for wavelengths longer than 200 nm were attributable to either Ln- or defect related centers, which corroborate the fact that they have a bandgap higher than 8.0 eV. The absorption band around wavelength, 275 nm, corresponds to defect absorption related to  $PO_3$  centers and/or oxygen vacancies. The hosts can potentially be used to study and interpret unperturbed rare earth emissions due to absence of host related absorption above 300 nm. The information presented herein is expected to serve as a library of absorption spectra for geologists, physicists, material scientists, and chemists working in the field of rare earths.

**Keywords:** orthophosphate; lanthanide; monazite/xenotime-structure; absorption spectra

## 1. Introduction

The lanthanide ( $Ln$ ) or rare earth element (REE) are f-block elements in the periodic table which can be subdivided into two categories, namely light  $Ln$  (La–Gd) and heavy  $Ln$  (Tb–Lu).  $Ln$  concentration in nature between 10–300 ppm can be considered to be a primary source for their extraction, and almost all the  $Ln$  ions are extracted from monazite, xenotime, and bastnäsites [1,2]. Light  $Ln$  being the most abundant, are found at concentrations among the highest compared to other commodities in many primary deposits. Conversely, heavy  $Ln$  are much less abundant, similar to rare metals (Sn, W, Ta) and are therefore much rarer in natural deposits.  $Ln$  are frequently incorporated into the crystalline network of carbonates, oxides, silicates, or phosphates together with other more common chemical elements but the mineral industry can only valorize a limited number of  $Ln$  minerals: bastnäsite (fluorocarbonate), monazite and xenotime (phosphates), and loparite (oxide).  $Ln$  have also been mined from apatite in Russia and South Africa, but this production has been extremely limited. Except for the xenotime which may be enriched in heavy  $Ln$ , all these minerals are essentially characterized by an enrichment in light  $Ln$ . Bastnäsite is the main  $Ln$  ore and is mainly extracted from

Chinese mines as well as from Mountain Pass in the United States until recently. The extraction of  $Ln$  from bastnäsite is primarily carried out by acid dissolution followed by solvent extraction and ion exchange methods. Another major source of  $Ln$  ions is monazite with nearly similar concentration of lighter  $Ln$  ions but with variable heavy  $Ln$  concentrations. Monazite occurs in a wide span of geological environment and known deposits are found worldwide [2]. Since the 1970s, ionic clays and lateritic clays, have also become an important source of heavy  $Ln$  [3]. This production, only located in the south of China is allowed by a low labor cost, and relatively simple extraction processes such as by in situ leaching with neutral or acid solutions. Despite the great variety of deposits, only 5 types are exploited: carbonatites (48% of world production), deposits of alkaline magmatism (2%), ion clay deposits (36%) laterite deposits (12%) and placers (2%). In 2018, world production was estimated at 170,000 t  $LnO$ . Apart from these primary sources, minerals such as apatite, calcium fluorophosphates, silico-phosphates, vanado-phosphates, and arseno-phosphates also contain  $Ln$  ions in very low concentration and can be used to extract them but large scale extraction procedures are still in development.

One of the important rare earth sources,  $Ln$  orthophosphates ( $LnPO_4$ ), are ceramic materials with interest in various application domains such as for luminescence-based temperature sensing [4], solid state lighting devices [5,6], geochronology [7], geothermometry [8,9], sensors and proton conductors [10], scintillators for X-ray and  $\gamma$ -ray detection-based medical imaging [11], catalysts [12], thermoluminescent phosphors [13], and laser hosts [14]. They also possess high durability and radiation damage resistance properties and thus are considered in nuclear waste management as potential immobilization matrices for minor actinides and plutonium [15,16]. Their natural analogues can contain significant amounts of actinides up to 50 wt. % of Th and U without harming their crystalline structure over geological time scales [17–20]. The  $LnPO_4$  can be prepared through various synthesis routes which includes, but not limited to, the precipitation reaction (homogeneous mixing of solutions), high temperature solid state reaction, and solvo-thermal reactions, due to simplicity and better controllability as well as rapidness of the product formation [2]. However, to use them for practical application such as to validate them as model systems, one needs to investigate their single crystals. The advantage with single crystal samples is the absence of defects associated with grain boundaries and absence of entropic effects which otherwise favour imperfection in the microstructure of the monocrystals, such as impurities, inhomogeneous strain and crystallographic defects such as dislocations [21].

In this context, the aim of the present study is to collect and present results on the UV-Visible absorption spectra of  $LnPO_4$  single crystal samples. The samples are obtained from the Smithsonian standard library, US. The samples are generally used for electron microprobe analysis (EMPA). The Smithsonian standard library contains absorption spectra of these samples at wavelengths  $>350$  nm. Hence, the present results on one hand will provide additional information for the Smithsonian library, and on the other hand, will act as a library of reference spectra for the end users. We study the UV-Visible absorption spectra in the wavelength region, 190–920 nm, for these single crystal samples to overlap, and extend the existing database of absorption spectra for all the  $LnPO_4$  samples.

## 2. Materials and Methods

### 2.1. Single Crystal Growth

The single crystal samples of  $LnPO_4$  ( $Ln = La-Lu$ , except Pm) were prepared by flux technique at Oak Ridge National Laboratory, USA [22], in accordance with the synthesis procedure discussed in Ref. [23]. In a typical procedure,  $Ln$ -oxides are placed in tightly covered platinum crucibles containing lead (II) hydrogen phosphate,  $PbHPO_4$ , to form the flux matrix at the high temperature. This is followed by an annealing step at 1633 K for 16 h. The crucibles were quenched suddenly to room temperature after being cooled to 1173 K at a rate of 1 K/h. The crystals are later dissolved in  $HNO_3$  to

extract respective single crystal samples [22]. The samples are also known to possess some Pb impurity as discussed in Ref. [24], based on the quantitative analyses, using  $K\alpha$  X-ray line for Sc,  $L\alpha$  lines for Y and the other REE elements, and the  $M\alpha$  line for Pb. However, the homogeneity of the samples has been tested using the homogeneity index and the samples have been found to be consistent in rare earth content [25].

## 2.2. Instrumentation

The high resolution two-dimensional (2D) images of the single crystals were obtained on a confocal laser microscope model LEXT OLS4000 from (Olympus, Tokyo, Japan). The samples were illuminated through the objective and the same way back to the detector (bright field). Image mapping technique was used to combine several images laterally. The confocal microscope allows a sharp image over a wide z-range, which is not possible with a normal microscope. The room temperature absorption spectra were measured in the wavelength range, 190–920 nm, using a single beam photometer with diode array detector model number SPECORD S–600 UV/Vis spectrophotometer, at a resolution of 1 nm, procured from Analytik Jena AG, Germany. The unpolished samples were measured in the transmission mode using either 1.0 mm, 0.50 mm, or 0.25 mm sample holders prepared in-house. The lamp spectrum was calibrated in each case separately before measurements of the single crystal samples. The absorption data was converted to the absorption coefficient ( $\alpha$ ) by considering width of the samples obtained from the laser profile of the 2D images.

## 3. Results and Discussion

### 3.1. Surface Investigation

A confocal scanning laser microscope is used to obtain 2D images of different  $LnPO_4$  ( $Ln = La-Lu$ , except Pm) crystal surfaces using white light source for surface illumination, Figure 1. As the  $Ln$  ions are divided into light and heavy  $Ln$  for order number 1–7 and 8–14;  $LnPO_4$  can be categorized as light  $Ln$  bearing orthophosphates ( $La-Gd$ ) $PO_4$ , and heavy  $Ln$  bearing orthophosphates ( $Tb-Lu$ ) $PO_4$ . The profile from all the sample surfaces evince that the crystal growth is uniform, and the crystals possess rigid top surfaces, *cf.* Figure 1. The sample-type and corresponding dimensions for each of the sample are summarized in Table 1 (column 1 and 2). The surface for all the samples was hard and most of the crystals were rectangular in shape suggesting that the growth was favored in a particular direction under the influence of high temperature synthesis conditions.

### 3.2. Structural Evaluation

The variation of lattice parameters ( $a$ ,  $b$ ,  $c$ ) and volume ( $V$ ) of a unit cell for all the  $LnPO_4$  samples, where the atomic number increases from  $La \rightarrow Lu$ , are combined in Table 1 (column 3–6). The information is collected from Refs. [26–32]. It is to be remembered here that we have used same sample set in the present work.

With a general electronic configuration of  $[Xe]4f^n6s^2$  ( $n = 1-14$ ) for  $Ln$  ions, the electron enters the  $4f$  orbital, and except for La or Lu, all the elements have partially filled  $f$ -orbitals. Also, they are shielded from outside by  $s$ -orbitals leading to similar chemical properties for almost all the  $Ln$  ions. However, their nuclear charge is poorly shielded from the outermost electron leading to lanthanide contraction effect, i.e., there is a decrease in their atomic and ionic radii with an increasing atomic number. The decrease in ionic radii for different light and heavy  $Ln$  bearing orthophosphates are compared in Figure 2 using red colour and blue colour, respectively. The  $Ln$  bearing orthophosphate samples possess axial ratios around 1.125 (for  $a/b$ ) and 1.050 (for  $a/c$ ) for light  $Ln$  bearing samples. Similarly, for heavy  $Ln$  bearing orthophosphate samples the values are consistent at 1.000 and 0.875 for  $a/b$  and  $a/c$ , respectively.



**Figure 1.** 2D real-space images for light and heavy  $L_n$  bearing orthophosphate single crystal samples.  $\text{SmPO}_4$  [4],  $\text{EuPO}_4$  [5],  $\text{TbPO}_4/\text{DyPO}_4/\text{PrPO}_4$  [6]—Reproduced by permission of the PCCO Owner Societies.

**Table 1.** Comparison of crystal dimensions, lattice parameters, cell volume, space group and structure-types for all the  $L_n\text{PO}_4$  samples.

Sample	Dimensions ( $\mu\text{m}$ )	$a$ ( $\text{\AA}$ )	$b$ ( $\text{\AA}$ )	$c$ ( $\text{\AA}$ )	$V$ ( $\text{\AA}^3$ )	Space Group	Structure
$\text{LaPO}_4$ [26]	$3000 \times 2000$	6.825 (4)	7.057 (2)	6.482 (2)	303.900	$P2_1/n$	Monazite
$\text{CePO}_4$ [27]	$2200 \times 1750$	6.777 (3)	6.993 (3)	6.445 (3)	296.970	$P2_1/n$	Monazite
$\text{PrPO}_4$ [28]	$1000 \times 500$	6.741 (3)	6.961 (4)	6.416 (1)	292.60	$P2_1/n$	Monazite
$\text{NdPO}_4$ [28]	$2000 \times 1500$	6.722 (1)	6.933 (1)	6.390 (2)	289.30	$P2_1/n$	Monazite
$\text{SmPO}_4$ [29]	$750 \times 1000$	6.669 (1)	6.868 (2)	6.351 (1)	290.89	$P2_1/n$	Monazite
$\text{EuPO}_4$ [29]	$1500 \times 500$	6.639 (3)	6.823 (3)	6.318 (3)	294.81	$P2_1/n$	Monazite
$\text{GdPO}_4$ [29]	$2000 \times 1500$	6.621 (2)	6.823 (2)	6.310 (2)	276.40	$P2_1/n$	Monazite
$\text{TbPO}_4$ [30]	$850 \times 300$	6.940 (1)	6.940 (1)	6.068 (1)	292.26	$P4_1/amd$	Xenotime
$\text{DyPO}_4$ [30]	$1000 \times 400$	6.907 (2)	6.907 (2)	6.046 (2)	288.43	$P4_1/amd$	Xenotime
$\text{HoPO}_4$ [30]	$1500 \times 500$	6.882 (2)	6.882 (2)	6.025 (2)	285.36	$P4_1/amd$	Xenotime
$\text{ErPO}_4$ [31]	$1700 \times 250$	6.860 (1)	6.860 (1)	6.003 (1)	282.50	$P4_1/amd$	Xenotime
$\text{TmPO}_4$ [31]	$1200 \times 800$	6.839 (1)	6.839 (1)	5.986 (1)	280.00	$P4_1/amd$	Xenotime
$\text{YbPO}_4$ [31]	$1350 \times 650$	6.816 (2)	6.816 (2)	5.966 (2)	277.20	$P4_1/amd$	Xenotime
$\text{LuPO}_4$ [32]	$950 \times 400$	6.792 (2)	6.792 (2)	5.954 (2)	274.67	$P4_1/amd$	Xenotime

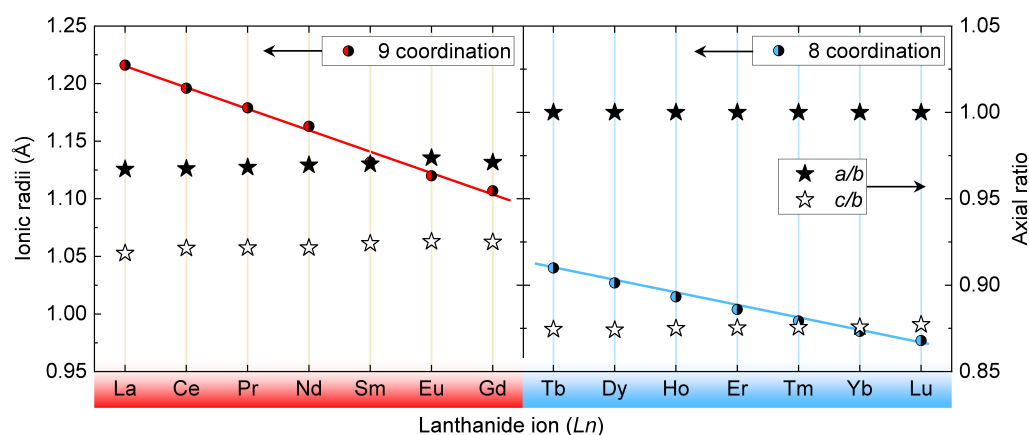


**Figure 2.** Variation of the  $L_n$  ionic radius (circles) and in the axial ratio (stars) for light  $L_n$  bearing orthophosphates with 9-coordination for light  $L_n$  ion (red colour), and heavy  $L_n$  bearing orthophosphates with 8-coordination ed  $L_n$  ions (blue colour). The axial ratios are calculated from the information published in Refs. [26–33].

The structural information for all the samples compiled in Table 1 (columns 7 and 8), show that there exists two different structures for light and heavy *Ln* bearing orthophosphate samples. The light *Ln* bearing samples possess  $P2_1/n$  space group with monoclinic *monazite*-structure ( $a \neq b \neq c$ ,  $\alpha = \gamma = 90^\circ$ ,  $\beta \sim 103\text{--}104^\circ$ ). On the other hand, the space group and structure for heavy *Ln* bearing orthophosphate samples is  $P4_1/amd$  and tetragonal *xenotime* ( $a = b \neq c$ ,  $\alpha = \beta = \gamma \sim 90^\circ$ ), respectively. The *monazite* orthophosphates possesses high thermal stability due to their compact structure which is made up of nine-coordinated  $LnO_9$  polyhedra of *Ln* ions, and  $PO_4$  tetrahedra, as shown in Figure 3(top).

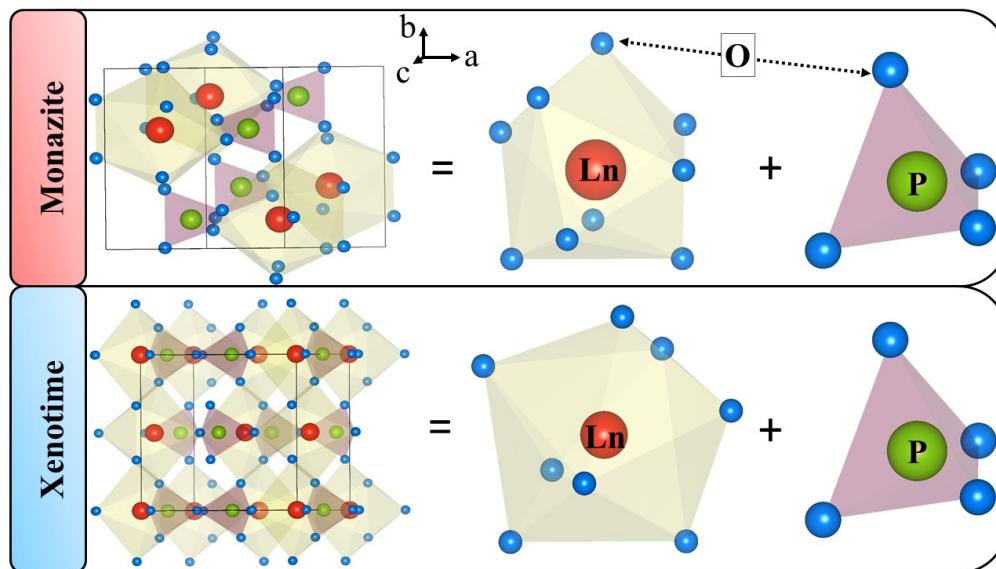


**Figure 3.** Comparison of crystal structures for light *Ln* (*monazite*) and heavy *Ln* (*xenotime*) bearing orthophosphate samples.

The *monazite* and *xenotime* orthophosphates are differentiated by crystallochemical partitioning, where the latter is formed by eight coordinated  $LnO_8$  polyhedra of *Ln* ion and  $PO_4$  tetrahedra, cf. Figure 3(bottom). Due to the greater ionic radius of La as compared to Lu, and a decrease in the ionic radii with an increasing atomic number for *monazite* orthophosphates, one corner of adjacent  $PO_4$  tetrahedra rotate towards the *Ln* ion transforming  $LnO_8$  to  $LnO_9$  polyhedra.

### 3.3. Absorption Spectra

The valence band of orthophosphates is mainly formed by 2s, 2p states of oxygen (O) atoms with an admixture of phosphorous (P) 3s, 3p orbitals, mirroring covalent bonding effects of P and O atoms. The *Ln* ions with 5s, 5p, 4f, 6s, 6p orbitals are mixed to the O states. The upper edge of the valence band is formed by O-2p and *Ln* 4f orbitals; the states of the lower edge of the conduction band are *Ln* 5d and P-3s, 3p orbitals [34].

#### 3.3.1. Light *Ln* Bearing Orthophosphates

##### LaPO<sub>4</sub> and GdPO<sub>4</sub>

The room temperature absorption spectra for LaPO<sub>4</sub> and GdPO<sub>4</sub> are shown in Figure 4A-a. The spectrum for LaPO<sub>4</sub> shows absorption around 205 and 274 nm. The absorption peak around 205 nm can be assigned to the  $PO_4^{3-}$  anions in accordance with an earlier report [35], while the absorption peak around 275 nm can be assigned to the defect related absorption in the host lattice. The nature of defect can be assigned to the charge transfer from an oxygen belonging to the  $PO_3$  center and/or an oxygen vacancy [35,36].

The absorption spectrum for GdPO<sub>4</sub> overlaps exactly with the one for LaPO<sub>4</sub>, *cf.* Figure 4A-a. The ionic radii for La<sup>3+</sup> and Gd<sup>3+</sup> in 9-fold coordination are 1.216 and 1.107 Å, respectively [33]. For a change of ~9% in the ionic radius of the two Ln ions, no change in the absorption features could be noticed suggesting that the origin of absorption bands in the wavelength region, 190–300 nm, is same for the two cases. The absorption spectrum for YPO<sub>4</sub>:Gd<sup>3+</sup> and GdPO<sub>4</sub> have also been reported in Ref. [37]. One can expect narrow absorption lines between wavelength, 170–280 nm, due to Gd<sup>3+</sup> 4f–4f transitions. We also noticed similar transitions at 275 and 308 nm, which corresponds to <sup>8</sup>S<sub>7/2</sub> → <sup>6</sup>I<sub>J</sub> and <sup>6</sup>P<sub>7/2</sub>, respectively. The same have been marked in Figure 4B, where the energy level diagram for LREEs (in vacuum) is shown for better comparison and understanding of the absorption transitions. One also expects an absorption at 201 nm due to the absorption from the ground state <sup>8</sup>S<sub>7/2</sub> to an emitting level <sup>4</sup>G<sub>7/2</sub>. However, such transitions could not be resolved in our results probably due to low resolution of the instrument. The results for the absorption of the host lattice are presented in Refs. [38,39] based on the vacuum ultra-violet (VUV) excitation spectra. The peak host sensitization bands of LaPO<sub>4</sub> and GdPO<sub>4</sub> are very close to each other at 159 and 160 nm, suggesting that they both have almost similar band gap [39].

#### CePO<sub>4</sub>

The UV-visible absorption spectrum for CePO<sub>4</sub> shows large absorption between wavelength, 190–500 nm, as shown in Figure 4A-b. With a melting point of ~2000 °C, CePO<sub>4</sub> is one of the most stable orthophosphate which can exist in two different forms, low temperature synthesized CePO<sub>4</sub> · xH<sub>2</sub>O with a hexagonal structure [40], and high temperature synthesized CePO<sub>4</sub> with a monazite structure [41]. As reported in Ref. [41,42], the absorption bands for high temperature synthesized sample (similar to our sample) are observed at 273, 257, 240, 215, and 202 nm due to 4f → 5d<sub>(1–5)</sub> transitions, typical for Ce<sup>3+</sup> containing/doped materials. For an unperturbed Ce<sup>3+</sup> ion (in vacuum), the 5d<sup>1</sup> level is expected around 52,000 cm<sup>-1</sup> above the lowest lying Ce<sup>3+</sup> 4f levels. However, due to its presence in phosphate host, the red-shift (D) of the lowest 5d level of Ce<sup>3+</sup>, *i.e.*, 5d<sub>1</sub> is observed at ~12,700 cm<sup>-1</sup> above the ground state, *cf.* Figure 4B. The red-shift is calculated using relation, D = Energy of free ion – (1240/5d<sub>1</sub> energy). The spectrum for our samples also shows large absorption >300 nm. In another report [43], the absorption spectrum for rod-like microstructures synthesized through hydrothermal method showed similar absorption features as is observed for our case. The authors assigned such a shift to a change in the bandgap. However, a shift of band gap from ~8.0 eV from Ref. [41] to ~3.2 eV from Ref. [43] does not appear realistic for such a large absorption above wavelength, 300 nm (marked “unknown” in Figure 4A-b).

#### PrPO<sub>4</sub>

The absorption spectrum for PrPO<sub>4</sub> single crystal sample is shown in Figure 4A-c. PrPO<sub>4</sub> shows a strong absorption in the visible region as evinced by the green body colour of the sample. The results for a single crystal sample and PrPO<sub>4</sub> nanorods [44], are compared in our recent publication [6]. The absorption spectrum shows two set of transitions: (a) Pr<sup>3+</sup> 4f–4f transitions in the wavelength region, 440–500 nm (Pr<sup>3+</sup> <sup>3</sup>H<sub>4</sub> → <sup>3</sup>P<sub>2</sub> transition), and 580–610 nm (Pr<sup>3+</sup> <sup>3</sup>H<sub>4</sub> → <sup>1</sup>D<sub>2</sub> transition) as marked in Figure 4B for Pr<sup>3+</sup> in vacuum; and (b) two broad bands at 230 (O<sup>2-</sup> → Pr<sup>3+</sup> charge-transfer band) and 330 nm (Pr<sup>3+</sup> 4f–5d band). The position of 4f–4f transitions in single crystal and nanorod samples are observed in the same wavelength region. The reader is referred to Ref. [6] for further information.

#### NdPO<sub>4</sub>

The result of the room temperature absorption spectrum for NdPO<sub>4</sub> sample is shown in Figure 4A-d. The sample possesses a purple–red body colour, *cf.* Figure 1. It absorbs strongly in the green and yellow region of the electromagnetic spectrum. The sharp peaks are observed at 355, 455, 525, 580, 680, 748, and 865 nm matching closely with the absorption bands for Nd<sup>3+</sup> ion in

vacuum as shown in Figure 4B and also in Ref. [45]. These sharp absorption bands belong to the  $\text{Nd}^{3+}$  transitions in the 4f electronic shell from ground level  $^4I_{9/2}$  to higher 4f-levels, cf. Figure 4B. As with  $\text{Pr}^{3+}$ , a broad band overlaps  $\text{Nd}^{3+}$  4f–4f transitions around 365 nm. The lowest of  $\text{Pr}^{3+}$  4f state lies within bandgap in  $\text{LaPO}_4$ , while the lowest of  $\text{Pr}^{3+}$  is within conduction band when compared in the vacuum referred binding diagram (VRBE) for the two cases [39]. Furthermore, the position of  $\text{O}^{2-} \rightarrow \text{Nd}^{3+}$  charge transfer band around 250 nm matches well with the expected position in the present host as per VRBE diagram.

#### $\text{SmPO}_4$

The room temperature absorption spectra for  $\text{SmPO}_4$  sample is shown in Figure 4A-e.  $\text{SmPO}_4$  absorbs weakly in the blue and blue–green region. The spectrum exhibit two different transition types: (a) broad band for wavelength  $< 300$  nm; and (b) sharp features between 300–550 nm ( $\text{Sm}^{3+}$  4f–4f  $^6H_{5/2} \rightarrow$  higher multiplet transitions as marked in the energy level diagram, Figure 4B). The UV–Vis absorption spectrum for  $\text{SmPO}_4$  single crystal and nano powders from Ref. [46], are compared in our recent work [4]. In another report [47], no absorption band was observed for  $\text{SmPO}_4$  around 300 nm due to weak interactions between Sm and P ions. However, based on our investigations in Ref. [4], we infer that it is a culmination of multiple bands with the  $\text{O}^{2-} \rightarrow \text{Sm}^{3+}$  charge transfer absorption band around  $\sim 200$  nm, and at least one other defect related absorption band around  $\sim 250$  nm due to charge-transfer from an oxygen belonging to a  $\text{PO}_3^-$  center, and/or an oxygen vacancy [35,39,48]. The complexity in identification of absorption features of  $\text{Sm}^{3+}$  arises as the free-ion configuration of  $\text{Sm}^{3+}$  has 198 spin angular momentum (S), orbital angular momentum (L), and total angular momentum (J) states involving sextet, quartet, and doublet states. When such states experience crystal field, for example in C1 symmetry, each SLJ state splits into  $J \pm 1/2$  crystal sublevels to produce 2002 crystal states. To add to it, not all of these may participate in the absorption spectrum. The reader is referred to Ref. [4] for assignment of the absorption bands.

#### $\text{EuPO}_4$

The absorption spectrum for  $\text{EuPO}_4$  is shown in Figure 4A-f. The samples possesses two broad bands at 223 and 278 nm, along with other sharp lines in the near–UV and blue region. In the published work of Ref. [35], the peak absorption for  $\text{PO}_4^{3-}$  is observed at  $\sim 160$ –200 nm, and the absorption longer than 200 nm (235 and 267 nm), could only be attributed to the rare earth/defect absorption. For our case, the sharp absorption lines at 316, 396, and 522 nm as also marked in the energy level diagram in Figure 4B, can be attributed to the *intraconfigurational*  $\text{Eu}^{3+}$  f–f transitions, while the other bands at 223 and 278 nm could be assigned to the  $\text{O}^{2-} \rightarrow \text{Eu}^{3+}$  charge–transfer and defect absorption, respectively. The reader is referred to Ref. [5] for further discussion on the absorption bands.

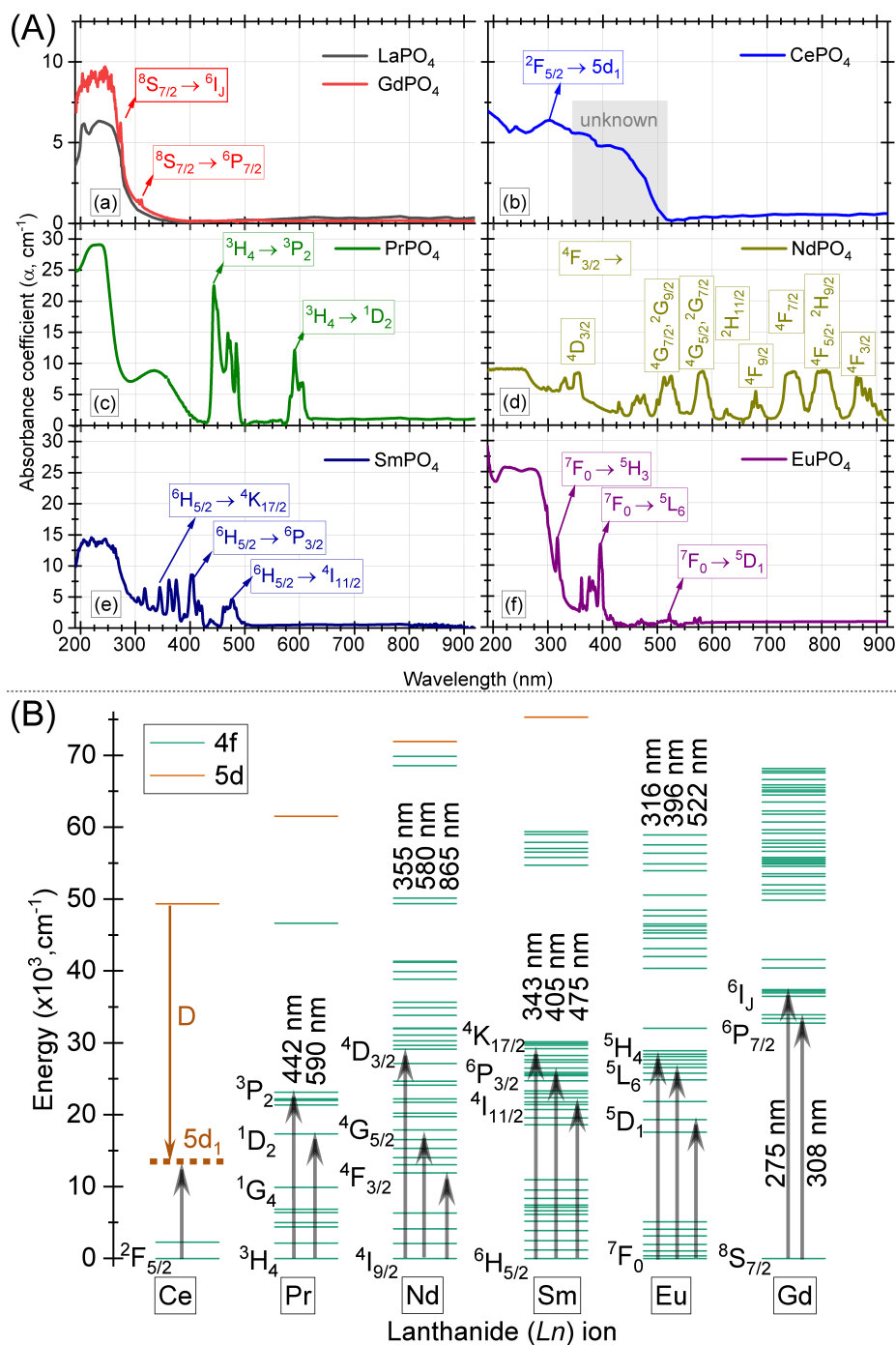


**Figure 4.** (A) The UV-visible absorption spectra for various light *Ln* bearing orthophosphates, (B) Energy level diagram for LREEs (in vacuum). The prominent absorption peaks are marked with upward arrows.

### 3.3.2. Heavy *Ln* Bearing Orthophosphates

#### TbPO<sub>4</sub>

The absorption spectrum at room temperature for TbPO<sub>4</sub> sample is shown in Figure 5A-a. The sample possess an off-white body colour. The absorption features between wavelength, 190–240 nm and 250–300 nm, can be assigned to the different spin-allowed and spin-forbidden  $4f^8 \rightarrow 4f^75d$  transitions of Tb<sup>3+</sup>, respectively [6,49,50]. The other transitions in the region, 300–500 nm,

are assigned to  $Tb^{3+}$  4f–4f transitions ( $^7F_6 \rightarrow$  higher multiplets). For example, the transitions at 352 and 490 could be marked for  $Tb^{3+}$   $^7F_6 \rightarrow ^5D_1$  and  $^5D_4$  respectively, cf. Figure 5B. The absorption features of  $TbPO_4$  in the VUV wavelength region, 140–160 nm, has been discussed and associated with the  $PO_4^{3-}$  anions in the recent publications [35,51], similar to the one observed for  $LaPO_4$  and  $GdPO_4$ . The reader is referred to Ref. [6] for a complete assignment of absorption bands.

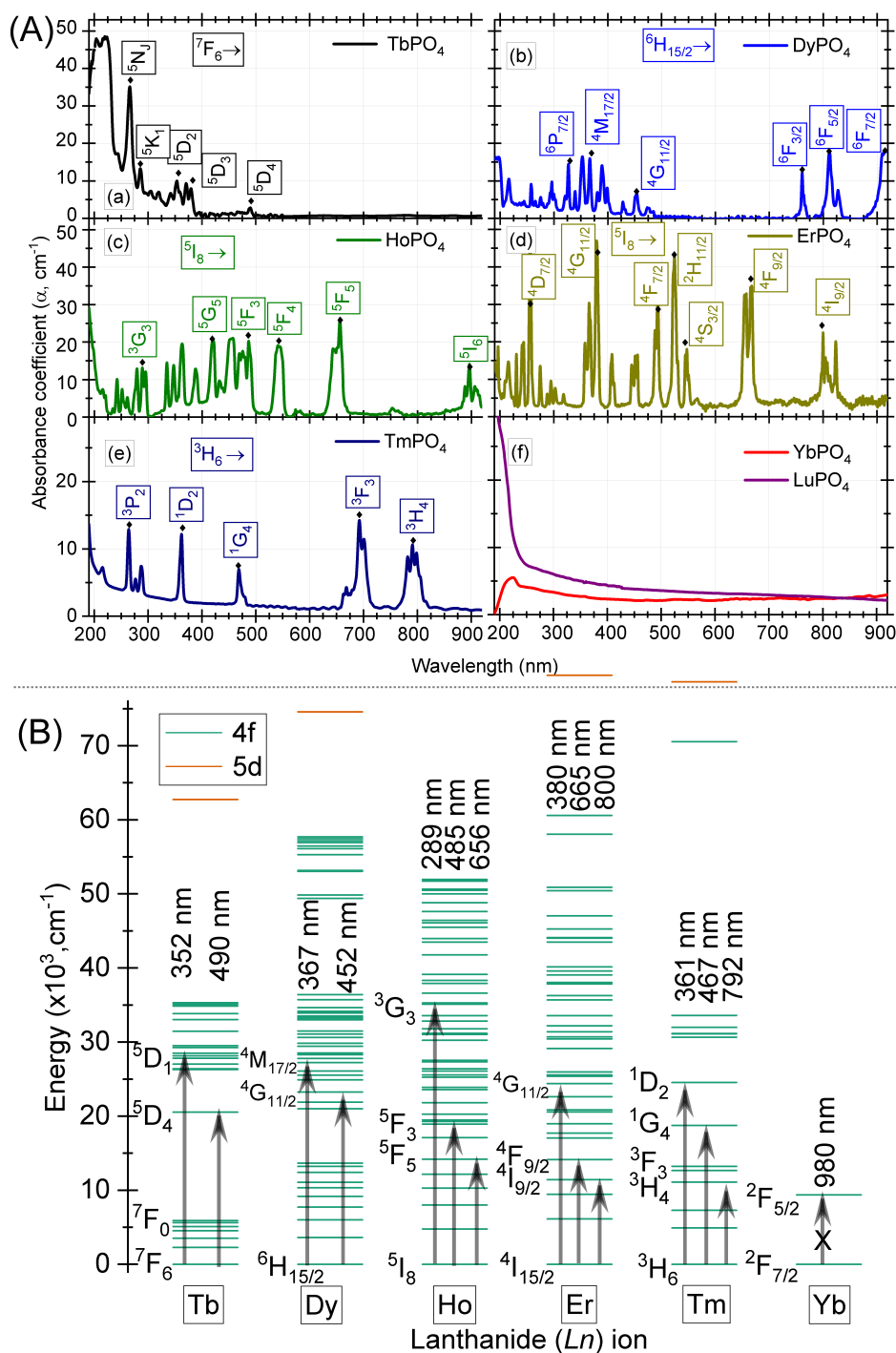


**Figure 5.** (A) The UV-visible absorption spectra for various heavy REE bearing orthophosphates; and (B) Energy level diagram for HREEs (in vacuum). The prominent absorption peaks are marked with upward arrows.

### DyPO<sub>4</sub>

The absorption spectrum for DyPO<sub>4</sub> sample is shown in Figure 5A-b. The sample possesses an ivory body color probably due to the lack of strong absorption in the visible region. The sharp line features are ascribed to the excitation from Dy<sup>3+</sup> <sup>6</sup>H<sub>15/2</sub> → higher electronic configuration (see Figure 5B), whereas the O<sup>2-</sup> → Dy<sup>3+</sup> charge-transfer band is expected around 170 nm on theoretical calculations using an expression by Jørgensen [52]. The range is beyond the detection range of our instrument and could not be observed in the absorption spectrum. The prominent transitions are marked in Figure 5B for free Dy<sup>3+</sup> ion (in vacuum), for better understanding and visualization of absorption transitions. The reader is also referred to Ref. [6] for further information.

### HoPO<sub>4</sub>

The absorption spectrum for HoPO<sub>4</sub> sample is shown in Figure 5A-c. The sample colour for HoPO<sub>4</sub> is beige. The sample possesses numerous lines in the visible and UV-region. The absorption spectrum shows lines typical of Ho<sup>3+</sup> which can be assigned to *intraconfigurational* 4f–4f absorption lines typically originating from the lowest level, <sup>5</sup>I<sub>8</sub>. More interestingly, no broad band is observed in the wavelength region, 250–300 nm, similar to the one observed for light rare earth bearing orthophosphates. This can be due to two reasons: (a) the light and heavy rare earth bearing samples possess different crystal structures leading to different crystal field effects; and (b) there is a increase in the bandgap among light and heavy rare earth bearing orthophosphates, for example, a change of 0.55 eV from LaPO<sub>4</sub> to LuPO<sub>4</sub> [39], which is expected to influence the position of 4f–5d bands in the absorption spectra. A similar observation is also made for other heavy rare earth bearing orthophosphates (please see next sections). The prominent Ho<sup>3+</sup> transitions at 289, 485, and 656 nm which belong to <sup>5</sup>I<sub>8</sub> → <sup>3</sup>G<sub>3</sub>, <sup>5</sup>F<sub>3</sub> and <sup>5</sup>F<sub>5</sub>, can be compared in Figure 5A-c and Figure 5B, respectively. Also, the complete assignment of the absorption bands is published in Ref. [53] for Ho<sup>3+</sup> doped YPO<sub>4</sub>. The sample also shows excellent photochromic properties as discussed in Ref. [54].

### ErPO<sub>4</sub>

The absorption spectrum for ErPO<sub>4</sub> sample is shown in Figure 5A-d along with energy level diagram for free Er<sup>3+</sup> ion (in vacuum) in Figure 5B. The absorption spectrum can be attributed to internal 4f–4f transitions of the configuration 4f<sup>11</sup> of the Er<sup>3+</sup> ion, from the ground state <sup>4</sup>I<sub>15/2</sub> to higher excited states. For example, the transitions at 380, 665 and 800 nm could be assigned to <sup>4</sup>I<sub>15/2</sub> → <sup>4</sup>G<sub>11/2</sub>, <sup>4</sup>F<sub>9/2</sub>, and <sup>4</sup>I<sub>9/2</sub> transitions respectively (see Figure 5B). The ErPO<sub>4</sub> sample possesses a pink colour probably due to strong absorption in the green region. By fitting the absorption spectral data using Judd–Ofelt model [36,55], Saltmarsh et al. predicted various radiative spectral properties such as radiative transition probability, fluorescence branching ratio and radiative decay time in Er<sup>3+</sup> doped LaPO<sub>4</sub> [56]. The spectrum for our sample (ErPO<sub>4</sub>) is found to be similar to the ones reported therein and can be compared to the one presented in Figure 5B.

### TmPO<sub>4</sub>

The absorption spectrum for TmPO<sub>4</sub> sample is shown in Figure 5A-e. The absorption spectrum shows sharp bands at 264, 361, 467, 693, and 792 nm. The bands can be attributed to the <sup>3</sup>H<sub>6</sub> → <sup>1</sup>P<sub>2</sub>, <sup>1</sup>D<sub>2</sub>, <sup>1</sup>G<sub>4</sub>, <sup>7</sup>F<sub>(2,3)</sub>, and <sup>3</sup>H<sub>4</sub> electronic transitions, as marked and compared for prominent cases in Figure 5B. The transitions are similar to one reported for Tm<sup>3+</sup> doped LaPO<sub>4</sub> [57]. Tm<sup>3+</sup> doped samples have found application in lasers, telecommunication and solar cells and is also known to produce upconversion luminescence in the visible region similar to Dy<sup>3+</sup> and Er<sup>3+</sup> ions. The energy level diagram and other details for the upconversion emission in Tm<sup>3+</sup> doped materials were reported in Ref. [58].

## YbPO<sub>4</sub> and LuPO<sub>4</sub>

The absorption spectra for YbPO<sub>4</sub> and LuPO<sub>4</sub> samples are shown in Figure 5A-f along with energy level diagram for free Yb<sup>3+</sup> ion (in vacuum) in Figure 5B. Both the samples are transparent in visible region with no absorption in the wavelength region, 250–750 nm. The spectrum is similar to the one observed for LaPO<sub>4</sub> and GdPO<sub>4</sub>. For Yb<sup>3+</sup> ions, one can expect absorption band around 975 nm (zero-phonon line) as the ion has only one excited state, <sup>2</sup>F<sub>5/2</sub>, located at about 10<sup>4</sup> cm<sup>-1</sup> above the ground state <sup>2</sup>F<sub>7/2</sub> through the Stark splitting of the sub-levels due to the crystal field in a crystalline environment of Yb ions [59]. However, no such transition was observed in our case due to instrumental limitation, and hence marked with a symbol X in upward arrow, *cf.* Figure 5B. For LuPO<sub>4</sub>, the absorption spectrum shows a dip in the spectrum around 200 nm, which can be assigned to the PO<sub>4</sub><sup>3-</sup> anions in accordance with Ref. [35].

## 4. Conclusions

In the present work, we present a comprehensive library of UV-Vis absorption transitions for technologically important rare earth orthophosphate samples. The host absorption for all the phosphates is expected to be in the VUV-region which lies outside the detection range of our experimental setup. However, the information for the bandgaps of LaPO<sub>4</sub>, GdPO<sub>4</sub>, LuPO<sub>4</sub> and YPO<sub>4</sub> can be obtained from the literature. The host exciton creation energy ( $E^{ex}$ ) for these hosts has been calculated in the literature using thermoluminescence investigations suggesting that the values are 8.00 eV (LaPO<sub>4</sub>), 8.05 eV (GdPO<sub>4</sub>), 8.55 eV (YPO<sub>4</sub>), 8.60 eV (LuPO<sub>4</sub>), respectively. Similar values for  $E^{ex}$  can be obtained for other orthophosphate, CePO<sub>4</sub> and Eu/TbPO<sub>4</sub>. By combining this information, we can infer following major observations from the present results:

1. All the orthophosphates can be categorized with either *monazite* or *xenotime* structure for light and heavy bearing  $LnPO_4$  hosts, respectively.
2. All the orthophosphates have a bandgap greater than 8.00 eV, with a change of ~0.60 eV for LuPO<sub>4</sub> when compared to LaPO<sub>4</sub>.
3. The PO<sub>4</sub><sup>3-</sup> does not absorb wavelengths >200 nm with a peak absorption ~180 nm. The absorption peak around 275 nm as observed mostly for light rare earth bearing orthophosphates, can be assigned to the defect absorption in the host lattice (charge transfer from an oxygen belonging to PO<sub>3</sub> center and/or oxygen vacancy).
4. The orthophosphate system can be considered to be an ideal system to study and compare absorption spectra of rare earth ions as the samples possess no absorption features >300 nm due to any other factors except that of  $Ln$  ions, *cf.* Figures 4A and 5A.
5. Some of the orthophosphates were already explored for numerous applications and the host possesses a fantastic opportunity for researchers working in the field.
6. For the  $LnPO_4$  hosts, where the oxygen atoms are covalently bonded within the phosphate group, the luminescence efficiency is expected to be much lower. This is due to inherently higher saturation of charge within the PO<sub>4</sub> groups when compared to a single oxygen atom whose 2p shells remain unfilled in an ionic matrix.

**Author Contributions:** Conceptualization, S.K.S.; methodology, S.K.S., T.B., T.K.; software, S.K.S., T.B., T.K., J.B.; formal analysis, S.K.S.; investigation, S.K.S.; resources, R.G. and J.H.; writing—original draft preparation, S.K.S.; writing—review and editing, all authors; supervision, R.G. and J.H. All authors have read and agreed to the published version of the manuscript.

**Funding:** This research was funded by EIT RawMaterials grant number 16304.

**Acknowledgments:** The authors thank the Smithsonian library, US, for providing samples with catalog # NMNH 168484 to NMNH168499 (16 samples), and Margret Fuchs for providing them to the corresponding author.

**Conflicts of Interest:** The authors declare no conflict of interest.

## References

1. Haque, N.; Hughes, A.; Lim, S.; Vernon, C. Rare Earth Elements: Overview of Mining, Mineralogy, Uses, Sustainability and Environmental Impact. *Resources* **2014**, *3*, 614–635. [[CrossRef](#)]
2. Achary, S.; Bevara, S.; Tyagi, A. Recent progress on synthesis and structural aspects of rare-earth phosphates. *Coord. Chem. Rev.* **2017**, *340*, 266–297. [[CrossRef](#)]
3. Bao, Z.; Zhao, Z. Geochemistry of mineralization with exchangeable REY in the weathering crusts of granitic rocks in South China. *Ore Geol. Rev.* **2008**, *33*, 519–535. [[CrossRef](#)]
4. Sharma, S.K.; Beyer, J.; Gloaguen, R.; Heitmann, J. Non-quenching photoluminescence emission up to at least 865 K upon near-UV excitation in a single crystal of orange-red emitting SmPO<sub>4</sub>. *Phys. Chem. Chem. Phys.* **2019**, *21*, 25669–25677. [[CrossRef](#)]
5. Sharma, S.K.; Kohler, T.; Beyer, J.; Fuchs, M.; Gloaguen, R.; Heitmann, J. Extending the temperature sensing range using Eu<sup>3+</sup> luminescence up to 865 K in a single crystal of EuPO<sub>4</sub>. *Phys. Chem. Chem. Phys.* **2019**, *21*, 16329–16336. [[CrossRef](#)]
6. Sharma, S.K.; Beyer, J.; Gloaguen, R.; Heitmann, J. Comparing the optical properties and thermal stability of green (TbPO<sub>4</sub>), yellow (DyPO<sub>4</sub>), and red (PrPO<sub>4</sub>) emitting single crystal samples. *Phys. Chem. Chem. Phys.* **2020**, *22*, 10247–10255. [[CrossRef](#)]
7. Williams, M.L.; Jercinovic, M.J.; Hetherington, C.J. Microprobe Monazite Geochronology: Understanding Geologic Processes by Integrating Composition and Chronology. *Annu. Rev. Earth Planet. Sci.* **2007**, *35*, 137–175. [[CrossRef](#)]
8. Andrehs, G.; Heinrich, W. Experimental determination of REE distributions between monazite and xenotime: potential for temperature-calibrated geochronology. *Chem. Geol.* **1998**, *149*, 83–96. [[CrossRef](#)]
9. Mogilevsky, P. On the miscibility gap in monazite–xenotime systems. *Phys. Chem. Miner.* **2007**, *34*, 201–214. [[CrossRef](#)]
10. Yu, R.; De Jonghe, L.C. Proton-Transfer Mechanism in LaPO<sub>4</sub>. *J. Phys. Chem. C* **2007**, *111*, 11003–11007. [[CrossRef](#)]
11. Lempicki, A.; Berman, E.; Wojtowicz, A.J.; Balcerzyk, M.; Boatner, L.A. Cerium-doped orthophosphates: New promising scintillators. *IEEE Trans. Nucl. Sci.* **1993**, *40*, 384–387. [[CrossRef](#)]
12. Onoda, H.; Nariai, H.; Moriwaki, A.; Maki, H.; Motooka, I. Formation and catalytic characterization of various rare earth phosphates. *J. Mater. Chem.* **2002**, *12*, 1754–1760. [[CrossRef](#)]
13. Ratnakaram, Y.; Naidu, D.T.; Vijayakumar, A.; Rao, J. Studies on optical absorption and luminescence properties of Dy<sup>3+</sup> doped mixed alkali borate glasses. *Opt. Mater.* **2004**, *27*, 409–417. [[CrossRef](#)]
14. Laporta, P.; Taccheo, S.; Longhi, S.; Svelto, O.; Svelto, C. Erbium-ytterbium microlasers: optical properties and lasing characteristics. *Opt. Mater.* **1999**, *11*, 269–288. [[CrossRef](#)]
15. Ewing, R.C. Metamict mineral alteration: An implication for radioactive waste disposal. *Science* **1976**, *192*, 1336–1337. [[CrossRef](#)]
16. Neumeier, S.; Arinicheva, Y.; Ji, Y.; Heuser, J.M.; Kowalski, P.M.; Kegler, P.; Schlenz, H.; Bosbach, D.; Deissmann, G. New insights into phosphate based materials for the immobilisation of actinides. *Radiochim. Acta* **2017**, *105*. [[CrossRef](#)]
17. Ewing, R.C.; Wang, L. Phosphates as Nuclear Waste Forms. *Rev. Mineral. Geochem.* **2002**, *48*, 673–699. [[CrossRef](#)]
18. Stoll, W. Thorium and Thorium Compounds. In *Ullmann's Encyclopedia of Industrial Chemistry*; American Cancer Society: Atlanta, GA, USA, 2000. [[CrossRef](#)]
19. Lumpkin, G.; Geisler-Wierwille, T. 5.22—Minerals and Natural Analogues. In *Comprehensive Nuclear Materials*; Konings, R.J., Ed.; Elsevier: Oxford, UK, 2012; pp. 563–600. [[CrossRef](#)]
20. Ji, Y.; Kowalski, P.M.; Kegler, P.; Huittinen, N.; Marks, N.A.; Vinograd, V.L.; Arinicheva, Y.; Neumeier, S.; Bosbach, D. Rare-Earth Orthophosphates From Atomistic Simulations. *Front. Chem.* **2019**, *7*, 197. [[CrossRef](#)]
21. Yang, G.; Park, S.J. Deformation of Single Crystals, Polycrystalline Materials, and Thin Films: A Review. *Materials* **2019**, *12*, 2003. [[CrossRef](#)]
22. Jarosewich, E.; Boatner, L.A. Rare-Earth Element Reference Samples for Electron Microprobe Analysis. *Geostand. Newsl.* **1991**, *15*, 397–399. [[CrossRef](#)]
23. Feigelson, R.S. Synthesis and Single-Crystal Growth of Rare-Earth Orthophosphates. *J. Am. Ceram. Soc.* **1964**, *47*, 257–258. [[CrossRef](#)]

24. Donovan, J.J.; Hanchar, J.M.; Picolli, P.M.; Schrier, M.D.; Boatner, L.A.; Jarosewich, E. Contamination in the Rare-Earth Element Orthophosphate Reference Samples. *J. Res. Natl. Inst. Stand. Technol.* **2002**, *107*, 693–701. [[CrossRef](#)] [[PubMed](#)]
25. Jarosewich, E.; Nelen, J.; Norberg, J.A. Reference Samples for Electron Microprobe Analysis. *Geostand. Newsl.* **1980**, *4*, 43–47. [[CrossRef](#)]
26. Mullica, D.; Milligan, W.; Grossie, D.A.; Beall, G.; Boatner, L. Ninefold coordination LaPO<sub>4</sub>: Pentagonal interpenetrating tetrahedral polyhedron. *Inorg. Chim. Acta* **1984**, *95*, 231–236. [[CrossRef](#)]
27. Beall, G.; Boatner, L.; Mullica, D.; Milligan, W. The structure of cerium orthophosphate, a synthetic analogue of monazite. *J. Inorg. Nucl. Chem.* **1981**, *43*, 101–105. [[CrossRef](#)]
28. Mullica, D.; Grossie, D.A.; Boatner, L. Structural refinements of praseodymium and neodymium orthophosphate. *J. Solid State Chem.* **1985**, *58*, 71–77. [[CrossRef](#)]
29. Mullica, D.F.; Grossie, D.A.; Boatner, L.A. Coordination geometry and structural determinations of SmPO<sub>4</sub>, EuPO<sub>4</sub> and GdPO<sub>4</sub>. *Inorg. Chim. Acta* **1985**, *109*, 105–110. [[CrossRef](#)]
30. Milligan, W.; Mullica, D.; Beall, G.; Boatner, L. The structures of three lanthanide orthophosphates. *Inorg. Chim. Acta* **1983**, *70*, 133–136. [[CrossRef](#)]
31. Milligan, W.O.; Mullica, D.F.; Beall, G.W.; Boatner, L.A. Structures of ErPO<sub>4</sub>, TmPO<sub>4</sub>, and YbPO<sub>4</sub>. *Acta Crystallogr. Sect. C* **1983**, *39*, 23–24. [[CrossRef](#)]
32. Milligan, W.; Mullica, D.; Beall, G.; Boatner, L. Structural investigations of YPO<sub>4</sub>, ScPO<sub>4</sub>, and LuPO<sub>4</sub>. *Inorg. Chim. Acta* **1982**, *60*, 39–43. [[CrossRef](#)]
33. Shannon, R.D. Revised effective ionic radii and systematic studies of interatomic distances in halides and chalcogenides. *Acta Crystallogr. Sect. A* **1976**, *32*, 751–767. [[CrossRef](#)]
34. Shchapova, Y.V.; Vinogradova, N.S.; Votyakov, S.L.; V.Ryzhkov, M. Chemical bonding and radiation stability of monazite-structure orthophosphates: Ab initio and spectroscopy studies. *Period. Mineral. ECMS* **2015**, 153–154. Available online: [http://periodicodimineralogia.it/doi/2015\\_ECMS\\_2015/ECMS\\_2015\\_Rome\\_Proceedings.pdf](http://periodicodimineralogia.it/doi/2015_ECMS_2015/ECMS_2015_Rome_Proceedings.pdf) (accessed on 9 July 2020).
35. Carrasco, I.; Piccinelli, F.; Romet, I.; Nagirnyi, V.; Bettinelli, M. Competition between Energy Transfer and Energy Migration Processes in Neat and Eu<sup>3+</sup>-Doped TbPO<sub>4</sub>. *J. Phys. Chem. C* **2018**, *122*, 6858–6864. [[CrossRef](#)]
36. Judd, B.R. Optical Absorption Intensities of Rare-Earth Ions. *Phys. Rev.* **1962**, *127*, 750–761. [[CrossRef](#)]
37. Sato, Y.; Kumagai, T.; Okamoto, S.; Yamamoto, H.; Kunimoto, T. Energy Transfer between Gd<sup>3+</sup> and Other Rare-earth Ions in GdPO<sub>4</sub> under Vacuum UV Excitation. *Jpn. J. Appl. Phys.* **2004**, *43*, 3456–3460. [[CrossRef](#)]
38. Nakazawa, E.; Shiga, F. Vacuum ultraviolet luminescence-excitation spectra of RPO<sub>4</sub>: Eu<sup>3+</sup> (R = Y, La, Gd and Lu). *J. Lumin.* **1977**, *15*, 255–259. [[CrossRef](#)]
39. Lyu, T.; Dorenbos, P. Charge carrier trapping processes in lanthanide doped LaPO<sub>4</sub>, GdPO<sub>4</sub>, YPO<sub>4</sub>, and LuPO<sub>4</sub>. *J. Mater. Chem. C* **2018**, *6*, 369–379. [[CrossRef](#)]
40. Lucas, S.; Champion, E.; Bregiroux, D.; Bernache-Assollant, D.; Audubert, F. Rare earth phosphate powders RePO<sub>4</sub> · nH<sub>2</sub>O (Re=La, Ce or Y)—Part I. Synthesis and characterization. *J. Solid State Chem.* **2004**, *177*, 1302–1311. [[CrossRef](#)]
41. Mayolet, A. Étude des Processus D'absorption et de Transfert D'énergie au Sein de Matériaux Inorganiques Luminescents Dans le Domaine UV et VUV. Ph.D. Thesis, Thèse de Doctorat Dirigée par Krupa, Jean-Claude Physique, Paris, France, 1995.
42. Chen, H.; Ni, Y.; Ma, X. Phase-controllable synthesis, shape evolution and optical performances of CePO<sub>4</sub> nanocrystals via a simple oil-bath route. *RSC Adv.* **2014**, *4*, 36553–36559. [[CrossRef](#)]
43. Palma-Ramírez, D.; Domínguez-Crespo, M.; Torres-Huerta, A.; Dorantes-Rosales, H.; Ramírez-Meneses, E.; Rodríguez, E. Microwave-assisted hydrothermal synthesis of CePO<sub>4</sub> nanostructures: Correlation between the structural and optical properties. *J. Alloys Compd.* **2015**, *643*, S209–S218. [[CrossRef](#)]
44. Lv, H.; Shen, X.; Ji, Z.; Chen, K.; Zhu, G. One-pot synthesis of PrPO<sub>4</sub> nanorods—Reduced graphene oxide composites and their photocatalytic properties. *New J. Chem.* **2014**, *38*, 2305–2311. [[CrossRef](#)]
45. Wang, Y.; Li, J.; Wang, J.; Han, S.; Guo, Y. Flux growth and characterizations of NdPO<sub>4</sub> single crystals. *J. Cryst. Growth* **2010**, *312*, 2779–2782. [[CrossRef](#)]
46. Cybinska, J.; Lorbeer, C.; Zych, E.; Mudring, A.V. Ionic liquid supported synthesis of nano-sized rare earth doped phosphates. *J. Lumin.* **2017**, *189*, 99–112. [[CrossRef](#)]

47. Babu, B.C.; Wang, G.G.; Baker, A.P.; Wang, B.L. Synthesis, photoluminescence, energy transfer and thermal stability of  $\text{SmPO}_4@ \text{SiO}_2: \text{Eu}^{3+}$  core-shell structured red phosphors for WLEDs. *J. Alloys Compd.* **2018**, *766*, 74–87. [[CrossRef](#)]
48. Shinde, K.N.; Dhoble, S.J.; Swart, H.C.; Park, K. *Some Novel Phosphate Phosphors*; Springer: Berlin, Germany, 2012; pp. 191–247. [[CrossRef](#)]
49. Runowski, M.; Grzyb, T.; Zep, A.; Krzyczkowska, P.; Gorecka, E.; Giersig, M.; Lis, S.  $\text{Eu}^{3+}$  and  $\text{Tb}^{3+}$  doped  $\text{LaPO}_4$  nanorods, modified with a luminescent organic compound, exhibiting tunable multicolour emission. *RSC Adv.* **2014**, *4*, 46305–46312. [[CrossRef](#)]
50. Wang, D.; Wang, Y. Optical properties of (Y,Tb)PO<sub>4</sub> under VUV excitation. *Mater. Chem. Phys.* **2009**, *115*, 699–702. [[CrossRef](#)]
51. Finke, B.; Schwarz, L.; Gurtler, P.; Kraas, M. Optical properties of potassium rare earth orthophosphates (RE = La, Ce, Tb). *Phys. Status Solidi A* **1992**, *130*, K125–K130. [[CrossRef](#)]
52. Jorgensen, C.K. Electron transfer spectra of lanthanide complexes. *Mol. Phys.* **1962**, *5*, 271–277. [[CrossRef](#)]
53. Becker, P.J.; Kahle, H.G.; Kuse, D. Absorption Spectrum and Zeeman Effect of  $\text{Ho}^{3+}$  in  $\text{YPO}_4$ . *Phys. Status Solidi* **1969**, *36*, 695–704. [[CrossRef](#)]
54. Wen, Q.; Xiao, S.; Gao, X.; Xia, W.; Yang, X. Photochromic effect of  $\text{HoPO}_4: \text{Li}^+$  powder. *Chin. Opt. Lett.* **2015**, *13*, 031601.
55. Ofelt, G.S. Intensities of Crystal Spectra of Rare-Earth Ions. *J. Chem. Phys.* **1962**, *37*, 511–520. [[CrossRef](#)]
56. Saltmarsh, N.; Kumar, G.; Kailasnath, M.; Shenoy, V.; Santhosh, C.; Sardar, D. Spectroscopic characterizations of Er doped  $\text{LaPO}_4$  submicron phosphors prepared by homogeneous precipitation method. *Opt. Mater.* **2016**, *53*, 24–29. [[CrossRef](#)]
57. Yang, S.H.; Yang, C.K.; Yan, J.H.; Lin, C.M. Improvement of the Luminescence of Red  $\text{LaPO}_4: \text{Eu}$  Nanophosphors for a Near-UV LED. *J. Electron. Mater.* **2014**, *43*, 3593–3600. [[CrossRef](#)]
58. Patra, A.; Ghosh, P.; Chowdhury, P.S.; Alencar, M.A.R.C.; Lozano B.W.; Rakov, N.; Maciel, G.S. Red to Blue Tunable Upconversion in  $\text{Tm}^{3+}$ —Doped  $\text{ZrO}_2$  Nanocrystals. *J. Phys. Chem. B* **2005**, *109*, 10142–10146. [[CrossRef](#)] [[PubMed](#)]
59. Nakazawa, E.; Shionoya, S. Cooperative Luminescence in  $\text{YbPO}_4$ . *Phys. Rev. Lett.* **1970**, *25*, 1710–1712. [[CrossRef](#)]

**Sample Availability:** The absorption spectra for all the samples can be provided upon request.



© 2020 by the authors. Licensee MDPI, Basel, Switzerland. This article is an open access article distributed under the terms and conditions of the Creative Commons Attribution (CC BY) license (<http://creativecommons.org/licenses/by/4.0/>).